2020

Microstructure evolution, lattice rotation retardation and grain orientation fragmentation in commercial purity aluminium deformed by high pressure torsion

Yu Liu
University of Wollongong

Cheng Lu
University of Wollongong, chenglu@uow.edu.au

Hui Wang
University of Wollongong, huiw@uow.edu.au

Anh Kiet Tieu
University of Wollongong, ktieu@uow.edu.au

Bin Liu
University of Wollongong, bl987@uowmail.edu.au

Microstructure evolution, lattice rotation retardation and grain orientation fragmentation in commercial purity aluminium deformed by high pressure torsion

Abstract

© 2020 The Authors. The behaviour of commercial purity aluminium processed by high pressure torsion is studied for a wide range of strains. The microstructure and texture are used to characterise the HPT deformation. Two different stages of microstructure evolution, i.e. grain fragmentation and grain elongation, are first found before attainment of steady state during HPT deformation. The grain fragmentation is not a linear function of shear strain in HPT. Significant grain refinement mainly occurs in the equivalent strain ranges of ~0 to 1 and ~11 to 32. Preferred simple shear orientations appear and vanish periodically due to the intrinsic instability of the shear direction in HPT. The lattice rotation of ultra-fine grain material is related to the grain size in the steady state. The strong ideal components have larger grain size than weak ideal components and non-ideal components. But the sensitivity of fragmentation to grain orientation tends to disappear as the steady state is attained.

Disciplines

Engineering | Science and Technology Studies

Publication Details

Liu, Y., Lu, C., Wang, H., Tieu, A. Kiet. & Liu, B. (2020). Microstructure evolution, lattice rotation retardation and grain orientation fragmentation in commercial purity aluminium deformed by high pressure torsion. Journal of Materials Research and Technology, 9 (3), 6642-6654.

Available online at www.sciencedirect.com

jmr&t Journal of Materials Research and Technology

www.jmrt.com.br

Original Article

Microstructure evolution, lattice rotation retardation and grain orientation fragmentation in commercial purity aluminium deformed by high pressure torsion

Yu Liu[a], Cheng Lu[a,*], Hui Wang[a,b], A. Kiet Tieu[a], Bin Liu[c,a]

[a] School of Mechanical, Materials, Mechatronic and Biomedical Engineering, University of Wollongong, Wollongong, NSW 2522, Australia
[b] Research Center for Advanced Science and Technology, The University of Tokyo, 153-0041, Japan
[c] School of Mechanical Engineering, Shijiazhuang Tiedao University, Shijiazhuang 050043, PR China

ARTICLE INFO

Article history:
Received 6 January 2020
Accepted 20 April 2020
Available online 16 May 2020

Keywords:
High pressure torsion
Aluminium
Microstructure evolution
Lattice rotation retardation
Grain orientation fragmentation.

ABSTRACT

The behaviour of commercial purity aluminium processed by high pressure torsion is studied for a wide range of strains. The microstructure and texture are used to characterise the HPT deformation. Two different stages of microstructure evolution, i.e. grain fragmentation and grain elongation, are first found before attainment of steady state during HPT deformation. The grain fragmentation is not a linear function of shear strain in HPT. Significant grain refinement mainly occurs in the equivalent strain ranges of ~0 to 1 and ~11 to 32. Preferred simple shear orientations appear and vanish periodically due to the intrinsic instability of the shear direction in HPT. The lattice rotation of ultra-fine grain material is related to the grain size in the steady state. The strong ideal components have larger grain size than weak ideal components and non-ideal components. But the sensitivity of fragmentation to grain orientation tends to disappear as the steady state is attained.

1. Introduction

According to the Hall-Petch relationship [1,2], grain size plays an important role in determining the properties of polycrystalline materials. Ultra-fine grained (UFG) or nanocrystalline (NC) materials generally show some excellent properties like high strength [3–5], improved ductility [6,7] and superplasticity [8–10] compared with the coarse-grained counterparts, without the need for changing the chemical composition. Extensive research has been carried out on various grain refinement techniques over the past several decades. However, the fabrication of UFG or NC materials is difficult when conventional plastic deformation processes are used, due to the low feasibility and high cost. Among the new methods to produce UFG or NC materials effectively, severe plastic deformation (SPD) techniques are becoming increasingly popular [11–14]. SPD methods are capable of inducing high plastic strains, resulting in highly refined grains. Among the SPD tech-

* Corresponding author.
E-mail: chenglu.uow@gmail.com (C. Lu).
https://doi.org/10.1016/j.jmrt.2020.04.056

niques, high pressure torsion (HPT) has a number of unique advantages. Specifically, compared with other SPD techniques, the HPT technique can offer extremely high continuous shear stain in one step. Therefore, HPT has recently attracted extensive research interest for various materials [15–18].

It is well known that the grain refinement process influences the evolution of microstructure. A number of studies on microstructure evolution have been undertaken to investigate the mechanism of grain refinement. Studies of different predominant mechanisms of plastic deformation in the ferrite and austenite in duplex stainless steel processed by HPT indicate that stacking-fault energy (SFE) is a key factor in determining the way of grain refinement [19]. Due to their superior ductility, aluminium (Al) and its alloys are widely used in investigations on HPT. In contrast to low-SFE materials in which twinning and de-twinning play an important role during plastic deformation, dislocation activity is the primary grain refinement mechanism in high-SFE materials such as Al. The microstructure evolution of HPT-processed Al can be roughly divided into two stages: (1) grain fragmentation stage and (2) steady-state stage [20]. In the steady-state stage, saturation of grain refinement and hardness is achieved. Thus this stage is also termed as the saturation stage, which is generally observed for strains $\varepsilon \geq 16$ in most cases [21]. The morphology of HPT-processed Al depends greatly on the direction of observation [22,23]. Most previous papers focus on the SD (shear direction)-RD (radial direction) plane and SPN (shear plane normal)-SD plane. The microstructure and texture evolutions on the SPN-RD plane have been rarely studies until now.

During plastic deformation, the fragmentation of parent grains is affected by their orientations. It has been reported that grain size with preferential orientation is larger in 50% cold-rolled copper [24]. A similar phenomenon was found in the experiment conducted by Raabe et al., in which the orientation gradient is prominent in the unstable texture component but absent in the stable orientation of cold-rolled iron [25]. Quantitative analysis of grain subdivision demonstrated different fragmentation behaviours for different orientations in cold-rolled Al. It has been observed that the orientation gradient is much larger in three non-ideal orientations while the grains with orientations close to stable β-fibres possess relatively small misorientations [26]. One of the potential mechanisms for the correlation between fragmentation behaviour and orientation is attributed to orientation symmetry [27]. Specifically, orientations aligned with the loading or sample symmetries are unstable during deformation. These orientations are prone to subdivision because they are located on the diverging lines of the velocity field and tend to rotate in two different directions. In addition to plane-strain deformation, the influence of orientation on grain fragmentation is also observed in torsional deformation. Naghdy et al. [28] have studied the dependence of grain size on the orientation in pure Al processed by HPT. It is found that the ideal components are generally larger than non-ideal components. However, the study has been limited at only one certain equivalent strain. Besides, the contrary fragmentation behaviour observed in the small grains has not been explained satisfactorily.

In the present work, as a widely used engineering material, 1050 Al alloy is processed by HPT at room temperature until grain refinement saturation. A full picture of the microstructure on the SPN-RD plane is revealed based on a quantitative analysis of the microstructure characteristics. Concurrently, the corresponding texture is analysed with the aim of revealing the relationship of texture evolution and grain size at the steady-state stage. Also, the influence of grain orientation on fragmentation with statistical significance is discussed in detail.

Table 1 – Chemical composition of Al 1050.

Element	Fe	Si	Mn	Mg	Ti	Zn	Cu	Al
Wt.%	0.31	0.06	0.04	0.01	0.02	0.04	0.02	Bal.

2. Experiment

2.1. Sample

The material used in the present work was Al 1050. Its chemical composition is given in Table 1. The original sample was in the form of an extruded rod with a diameter of ~15 mm. The diameter of the extruded rod was reduced to 10 mm on a lathe. Then the 10 mm diameter rod was cut into 1.5 mm thick discs using wire cutting. To obtain recrystallized grains, these discs were pre-annealed at a temperature of 300°C for 2 h, and then air-cooled.

2.2. HPT

The HPT device is manufactured by W. Klement GmbH (Lang, Austria). The discs were HPT-processed in a semi-constrained condition. The disc-shaped samples were placed in the die cavity between two anvils and were subjected to a compressive pressure of ~6 GPa at room temperature. The upper anvil was fixed and a torsional strain was imposed by rotating the lower anvil at 0.5 rpm. The low rotational speed can minimise the frictional heat generation [29,30]. In order to cover a wide range of shear strain, 9 different rotation angles were investigated: 15° (1/24 turn), 30° (1/12 turn), 45°(1/8 turn), 90° (1/4 turn), 180° (1/2 turn), 360° (1 turn), 720°(2 turns), 1080° (3 turns) and 1800° (5 turns). As shown in Fig. 1, in this study the HPT geometry is defined with RD, SD and SPN sample reference system.

2.3. EBSD

The microstructure and texture of the HPT-processed commercial purity (CP) Al were investigated using the Electron Backscatter Diffraction (EBSD) technique. The EBSD samples were mechanically ground and electro-polished. The EBSD scans were carried out at an accelerating voltage of 15 kV, at a working distance of 15 mm. The EBSD measurements were conducted on an axial cut plane, i.e. the SPN-RD plane, near the periphery and at a radial distance of 4 mm from the disc centre. The EBSD measurement area is shown schematically in Fig. 1 as a red rectangle. The scanned areas range from $150 \times 120\ \mu m^2$ to $50 \times 40\ \mu m^2$ with increasing strain. At high strains, the average grain size drops dramatically to about 0.6 μm. In order to acquire enough data points for a given grain, the corresponding scan step size decrease from 0.3 μm at low strains to 0.075 μm for high strain samples. The Bunge nota-

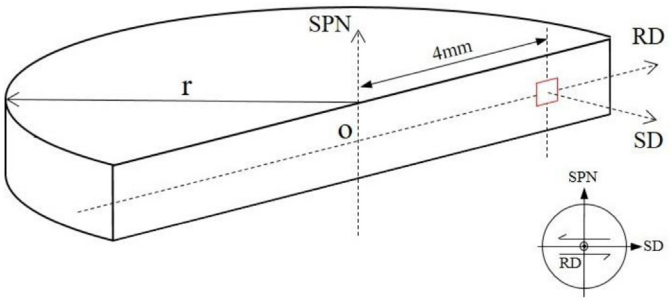

Fig. 1 – Schematic illustration of axial section of HPT disc. The EBSD measurement is conducted on SPN-RD plane, and the observed area is shown as a red rectangle.

tion is employed in the orientation distribution function (ODF) calculation. The reference frame for ODFs are X_0 || SD, Y_0 || SPN and Z_0 || RD in extrusion sample and HPT-processed samples.

The grain size is strongly influenced by the definition of grain boundary. In this study, high angle grain boundary (HAGB) refers to the grain boundary with misorientation angle $\theta \geq 15^\circ$, and low angle grain boundary (LAGB) is defined as the grain boundary with $2^\circ \leq \theta < 15^\circ$. HAGBs are highlighted by solid black lines and LAGBs are denoted by solid grey lines in the EBSD map.

2.4. *Equivalent strain*

The material deformation mode of HPT is usually classified as simple shear [31]. For this geometry, the shear strain distribution is symmetrical around the cylinder axis. The applied shear strain γ can be given by an equation in the idealized condition where the disc thickness (h) remains constant during HPT [32,33] :

$$\gamma = \frac{r\theta}{h} \quad (1)$$

where r is the distance from the disc centre, θ is the rotation angle, and h is the thickness of the disc.

The equivalent strain, ε, is given by the following expression if the disc thickness is assumed to be constant during torsional deformation after compression [34–37].

$$\varepsilon = \frac{\gamma}{\sqrt{3}} \quad (2)$$

Due to the shape of die cavity, the sample thicknesses at the EBSD measurement areas decrease to 1.349 mm after compression. In Table 2, the calculated equivalent strains of the HPT samples with different rotation angles (from 15° to 1800°) are listed. It should be noted that the actual equivalent strains vary slightly within the scanned areas and the calculated equivalent strains are applicable only at the mid-points of the scanned area. However, the deviations of equivalent strains between centre and edge of the scanned rectangles are less than 2%, which would not have significant influence on microstructure and texture analysis. Thus the equivalent strains listed in Table 2 could be considered as the equivalent strains of the entire rectangular scanned areas.

Table 2 – Equivalent strain values of the samples for different rotation angles at the positions of red rectangle shown in Fig. 1.

Sample No.	Rotation angle θ (deg.)	Shear strain γ	Equivalent strain ε
1	15	0.78	0.45
2	30	1.55	0.90
3	45	2.33	1.34
4	90	4.66	2.69
5	180	9.32	5.38
6	360	18.63	10.76
7	720	37.26	21.51
8	1080	55.89	32.27
9	1800	93.15	53.78

3. Results

3.1. *Microstructure and texture of as-annealed sample*

The inverse-pole figure (IPF) coloured EBSD map of the sample before deformation is shown in Fig. 2(a). The sample was cut from the rod deformed by extrusion along the SPN of the HPT sample coordinate system, so that the initial grains in the sample were elongated along the SPN. After annealing, some grains still maintain the elongated shape along the SPN, which can demonstrate the influence of compression on the grain aspect ratio during HPT.

It is widely thought that simple shear is the predominant deformation mode in HPT. The ideal texture components of simple shear in FCC materials are A* 1, A* 2, A/A_b, B/B_b and C [38,39] (A_b and B_b correspond to $\bar{A}$ and $\bar{B}$ in previous publications, respectively). Due to the monoclinic sample symmetry of HPT, A and B components are equivalent to A_b and B_b components respectively. All ideal simple-shear texture components and the Cube component are presented in the $\phi_2 = 45^\circ$ ODF section [40]. It is found that the Cube is the dominant orientation but a fraction of the C component exists after annealing as well. The positions of Cube and all ideal simple shear texture components in $\phi_2 = 45^\circ$ ODF section are shown in Fig. 2(c).

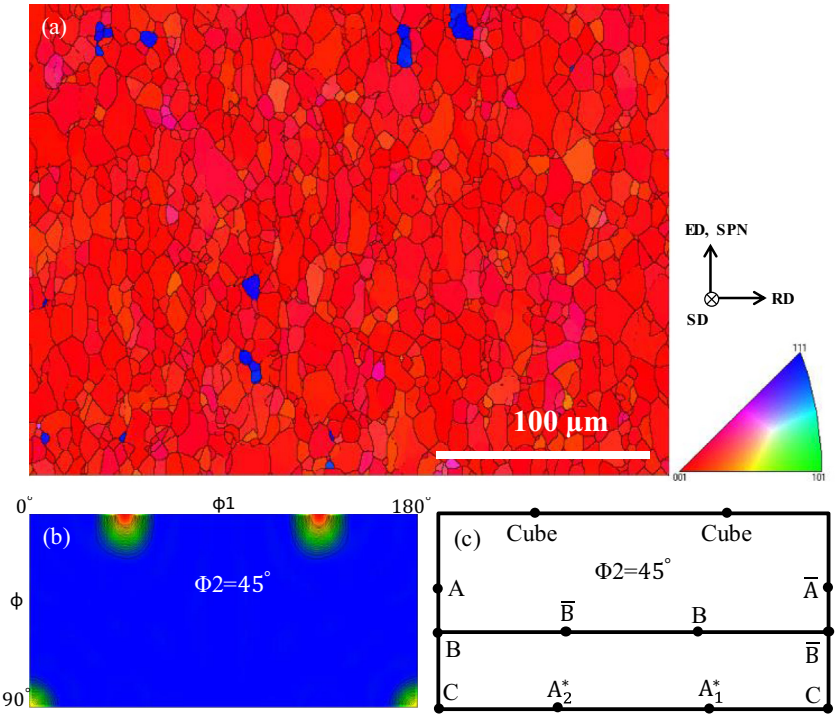

Fig. 2 – (a) IPF map of the extrusion sample after annealing, orientation colour code and sample reference system (b) ODF at the $\phi_2 = 45°$ ODF section and (c) ideal simple shear and Cube components marked on the $\phi_2 = 45°$ ODF section. ED, extrusion direction.

3.2. *Microstructure evolution*

The IPF-coloured EBSD maps in Fig. 3 demonstrate the microstructures of the specimens after HPT for an equivalent strain ε of up to 53.78. Individual grains are coloured according to crystal direction relative to the SPN direction. In these EBSD maps, the red colour stands for {100} <u v w> fibre, which represents the orientations whose [1 0 0] crystal directions are perpendicular to SPN. In this study, {100} <u v w> fibre mainly includes Cube and C components. The green and blue colours represent the {110} and {111} <u v w> fibres, respectively.

As shown in Figs. 3 (a), the initial grain structure is visible at most areas and the red colour fibre is still mainly prevalent at the strain $\varepsilon = 0.45$. However, a remarkable microstructural change is observed inside the grains. The increasing density of substructures and the wider colour range indicate developing substructures [23,41]. Specifically, a proliferation of LAGBs is seen at this stage. As the imposed strain increases, dislocation propagation gives rise to more opportunity for their mutual reactions to form dislocation tangles and walls. Subsequently the accumulation of the dislocation tangles and walls leads to the formation of the LAGBs observed in the EBSD maps. In addition, a number of newborn grains observed alongside their parent grains indicate the onset of grain refinement.

A significant change in morphology is observed when the strain $\varepsilon = 0.90$. A periodic colour spread is seen in most areas on the EBSD maps. The wider range of colours indicate that more severe grain distortion has taken place at this deformation stage. As can be seen in Fig. 3 (b), a band-shaped structure with irregular boundaries in place of the initial grain structure predominates in the morphology. Under simple shear deformation, the material flow line tends to align with the direction of the shear deformation in three-dimensional space [42]. As the HPT strain increases, the major axis of the grain parallel to the SPN inclines towards the flow line [22]. As a result, the grain thickness and size projected on the SPN-RD plane (i.e. on the EBSD maps) decreases. In addition, due to the compression and shear strain, the material flows along the RD-SD plane. Consequently, band-shaped structures are generated. Inside the grains, a higher density of LAGBs is seen due to continuous absorption of dislocations by dislocation walls at a higher shear strain. In contrast to the stage where the equivalent strain is 0.45, the LAGB-free areas almost vanish. Small newborn grains are found not only at the GBs but also inside the parent grains.

In comparison with the stage of equivalent strain $\varepsilon = 0.90$, it is found that the grain size is smaller when the strain $\varepsilon = 1.34$ (Fig. 3(c)). Some of the intra-granular LAGBs observed in the last deformation stage are transformed into HAGBs as the shear strain is increased. As a result, the band-shaped grains surrounded by the HAGBs are fragmented into smaller grains. These new grains are subjected to the shear strain and elongated into new band-shaped grains. As stated before, the colours on the EBSD map denote different crystallographic orientations. As the HPT deformation increases ($\varepsilon = 2.69$), the wider colour range represents further grain fragmentation. Close examination of Fig. 3(d) reveals that the band shape structures are fragmented into smaller structures, leading to

further decline in the grain size and aspect ratio. At the higher strain $\varepsilon = 5.38$, the structures generated from the fragmentation at the equivalent strain of 2.69 are elongated again along the RD, as shown in Fig. 3(e). It should be noted that the elongated structure as seen is only the projection of actual grains on the SPN-RD plane of observation. The 3-dimensional shape

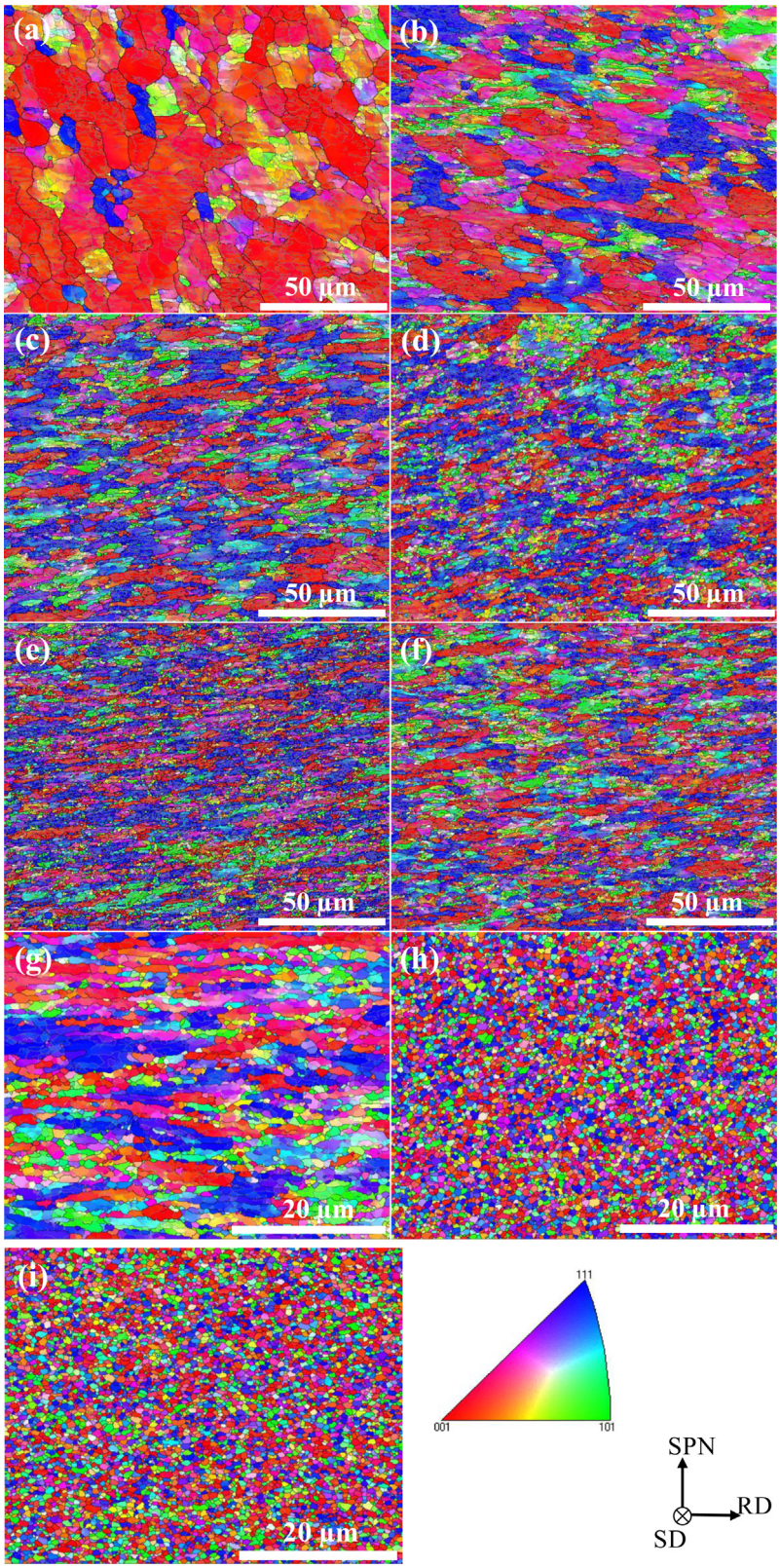

Fig. 3 – EBSD maps of samples after HPT at the equivalent strain of (a) 0.45, (b) 0.90, (c) 1.34, (d) 2.69, (e) 5.38, (f) 10.76, (g) 21.51, (h) 32.27 and (i) 53.78.

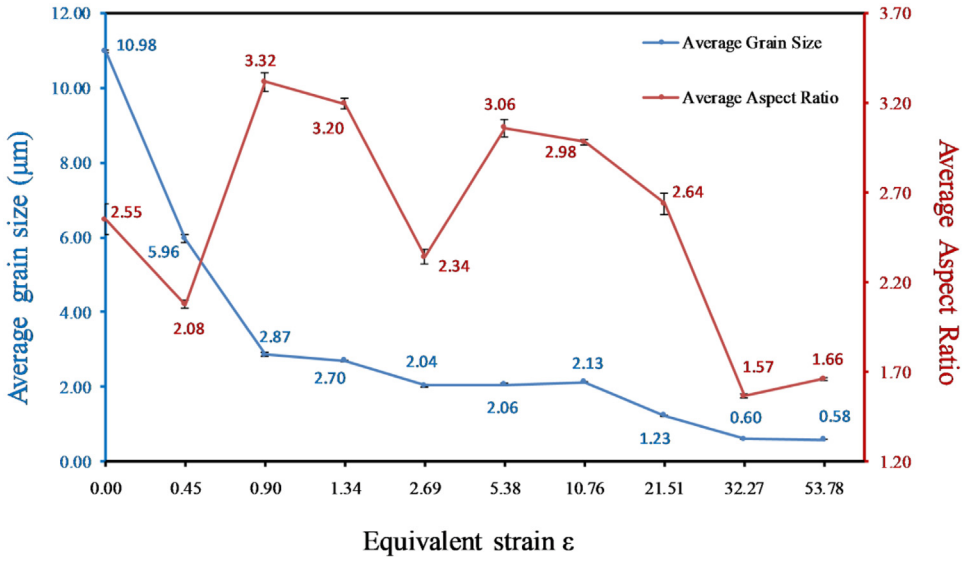

Fig. 4 – Average grain sizes and aspect ratios of the HPT samples at the same areas observed by EBSD.

of the real grain is shrunk along the SPN and stretched in the SD and RD during HPT.

As the equivalent strain ε increases to 10.76, as shown in Fig. 3 (f), it is interesting that highly elongated structures still predominate in the morphology, but the grain size seems to be larger than that at the equivalent strain of 5.38. This is consistent with previous observations in HPT [43,44], where the grains close to the centre of sample are smaller and more severely deformed while the highly strained grains at the periphery of disc are larger. It is believed that the grain growth at higher strains is associated with dynamic recrystallization [45] or GB migration [46–48]. As the equivalent strain ε increases to 21.51, many LAGBs can still be observed within the grains, but the interiors of the grains become cleaner. This indicates that some of the LAGBs are converted into HAGBs by absorbing dislocations progressively, causing a fall in the density of intra-granular LAGBs. As a result, the grain size shows a significant drop. However, the areas of agglomerates with close orientations imply that completely homogeneous microstructure and orientation have not been achieved at the stage. For the equivalent strains of 32.27 and 53.78, the morphology and the colour spreads are remarkably identical. This implies that a saturation in grain refinement has been achieved. The LAGBs observed at the equivalent strain of 21.51 continue to be converted to HGABs due to the greater imposed shear strain. As a consequence, new grains surrounded by HAGBs are generated. The grain size has reduced to the UFG scale. The grains are not band-shaped any longer. More and more grains become more equiaxed, and the microstructure distribution is near-homogenous in the two areas.

3.3. *Quantitative microstructure characteristics*

In this study, four parameters are used to quantitatively represent the characteristics of grain fragmentation and refinement: grain size, grain aspect ratio, misorientation angle distribution (MAD) curve and fractions of LAGBs and HAGBs. The grain size is calculated by the equivalent diameter of a fitted circle to a grain, and the grain aspect ratio is defined as the ratio of major to minor axis of a fitted ellipse. As shown in Fig. 4, the average grain size of the as-annealed sample is about 11 μm. As explained earlier, some of the initial grains are elongated along the SPN after annealing, resulting in an average aspect ratio of about 2.55.

The average grain size decreases sharply to 5.96 μm after processing by HPT at the strain $\varepsilon = 0.45$. However, as observed previously, the initial grain structure is retained to a large extent at this stage. The dramatic drop in grain size is attributed to the formation of small grains in the vicinity of GBs. The average aspect ratio shows a similar trend, decreasing moderately to 2.08. The drop in aspect ratio is associated with the applied compression along the SPN before the HPT rotation and the formation of newborn grains. As shown in Fig. 5 and Fig. 6, the relative frequency of HAGBs is extremely low (13.0%), and the curve peaks at a low misorientation angle of ~2°. The density of LAGBs is increased by absorbing dislocations at the accumulated strain ε of 0.90. The dislocation absorption will lead to an increase in the misorientation of neighbouring grains. As a result, the peak misorientation angle shows a shift towards a larger value. Concurrently, the fraction of HAGBs increases to 19.3%, which is related with the considerable generation of small grains. Thus the grain size has been significantly reduced to 2.87 μm. The corresponding aspect ratio increases to the maximum value of 3.32 due to the formation of band-shaped structures. The maximum of aspect ratio is approximately consistent with a previous result of Al torsional deformation [49].

With increasing deformation to equivalent strain levels of 1.34 and 2.69, both the grain size and the aspect ratio illustrate a slight downward trend due to grain fragmentation. Specifically, at the two stages, the average grain sizes decrease to 2.70 μm and 2.04 μm, while the aspect ratios reduce to 3.20 and 2.34 respectively. It can be seen from the MAD curves that LAGBs with low θ are progressively transferred into the LAGBs with high θ and the HAGBs via dislocation absorption at the former stage. As a result, the fraction of HAGBs is increased

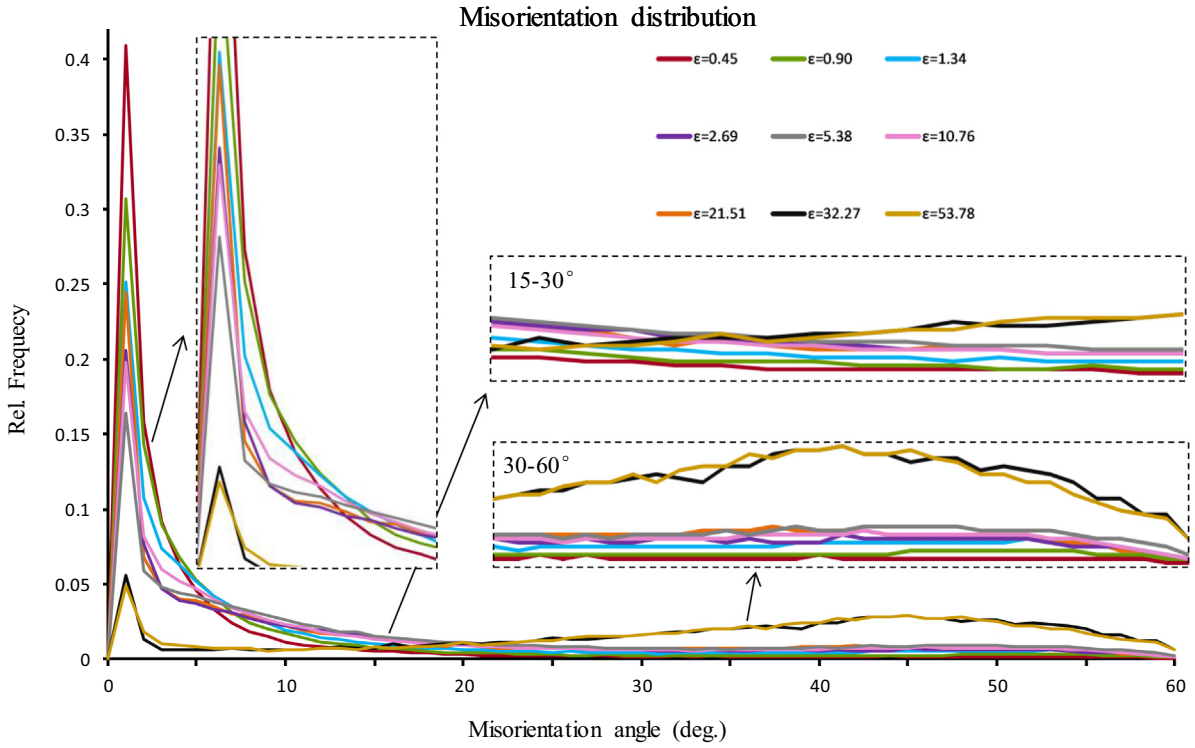

Fig. 5 – MADs of samples processed by HPT at the same areas of EBSD observation. The insets are the zoomed-in portions of MADs corresponding to different misorientation angles.

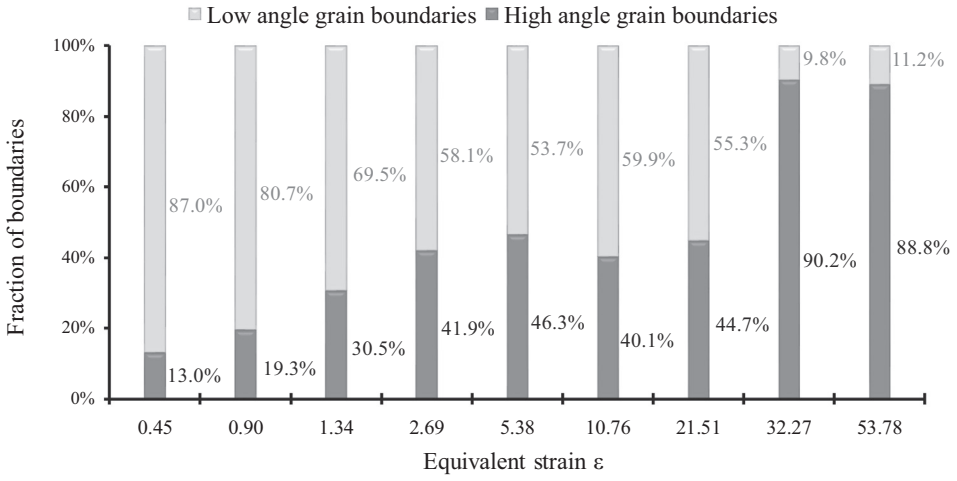

Fig. 6 – fractions of LAGBs and HAGBs at different deformation stages.

to 30.5%. The trend in the MAD curve continues until $\varepsilon = 21.51$. The growth in the fractions of LAGBs with relatively high θ (about 6°) and the HAGBs is accelerated, whereas the relative frequency of LAGBs with relatively low θ is reduced.

As the equivalent strain ε increases to 5.38, the grain size is stabilized within a narrow range, indicating no further grain fragmentation. The grains are not further refined even though the increase in strain at this stage is the same as the cumulative strain at all previous stages. Therefore, the relationship between the grain size and the strain is non-linear. Although no significant grain fracture takes place, a notable change in grain shape is observed. The aspect ratio rises dramatically to 3.06, which is due to the elongation of new grains born from the grain fragmentation at the equivalent strain of 2.69. The fraction of LAGBs declines to 53.7% but that of HAGBs increases, as LAGBs are transformed into HAGBs constantly with increasing deformation. In terms of morphology, the increase in fraction of HAGBs and stable grain size represent the most of new HAGBs generated at this stage are discontinuous.

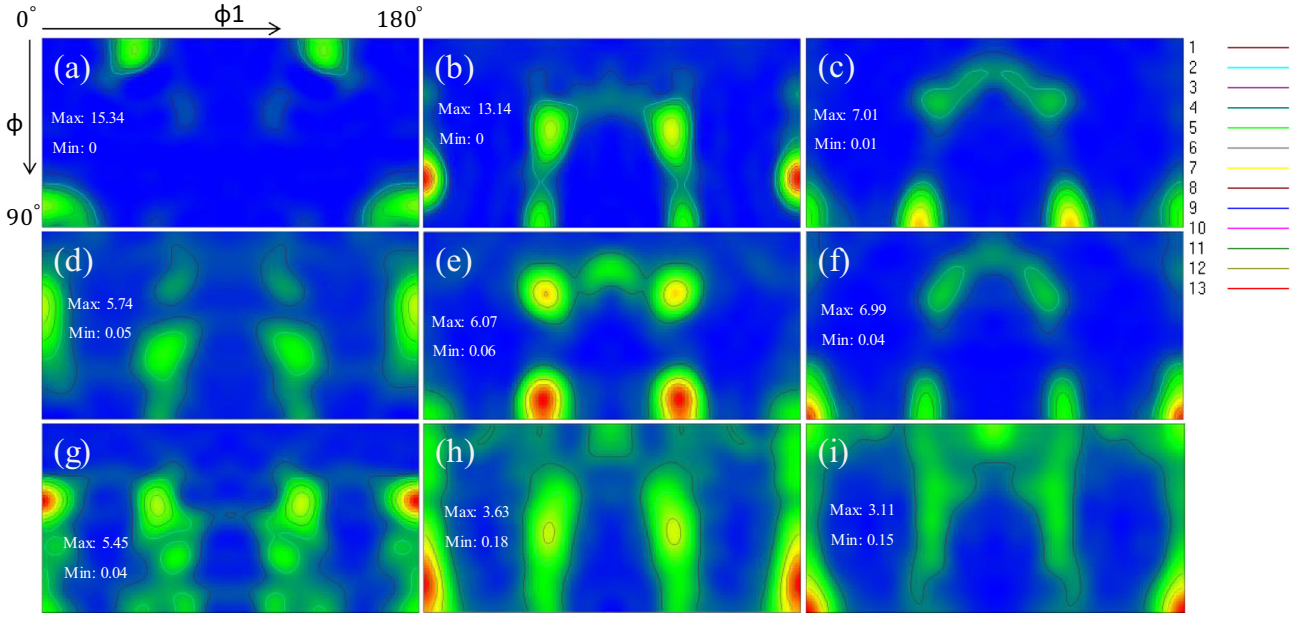

Fig. 7 – $\phi_2 = 45°$ ODF maps of the samples at the equivalent strain of (a) 0.45, (b) 0.90, (c) 1.34, (d) 2.69, (e) 5.38, (f) 10.76, (g) 21.51, (h) 32.27 and (i) 53.78.

The slight grain growth owing to dynamic recrystallization or GB migration occurs when the strain ε increases to 10.76. As a result, the consistent decline in grain size is reversed and the average grain size grows slightly from 2.06 μm to 2.13 μm. Concurrently, the average aspect ratio decreases to 2.98. During the process of GB growth, some grains grow at the expense of some other grains, causing a decrease in the number of grain boundaries. Therefore, the rising trend of the relative frequency of HAGBs does not continue at this stage. The fraction of HAGBs reduces to 40.1%. At the strain ε of 21.51, the conversion from LAGBs to HAGBs leads to the generation of new grains. It follows that both the grain size and aspect ratio decrease to 1.23 μm and 2.64, respectively. Close inspection reveals that the relative frequencies of HAGBs and LAGBs with low θ increase while the relative frequency of LAGBs with high θ drops drastically, denoting that the dislocation absorption by HAGBs is faster than by LAGBs at this stage.

As the strain ε increases to 32.27 and 53.78, the average grain sizes fall to the UFG level (600 nm and 580 nm, respectively). Besides, the average aspect ratios level out at about 1.6. It is found that the two parameters are stabilized at the two stages, indicating the saturation of grain refinement. The fractions of HAGBs increase rapidly to peak at the expense of LAGBs. Consequently, the fractions of LAGBs drop to about 10%. Bimodal distributions in MAD reveal two peaks at low (~2°) and high (~45°) misorientation angles.

3.4. *Texture evolution*

In Fig. 7, the $\phi_2 = 45°$ ODF sections demonstrate the texture evolution of the HPT discs deformed by up to 1800°. Volume fraction is a method of comparing textures [50]. Fig. 8 shows the volume fractions of ideal simple-shear texture components with an orientation tolerance of 10° at the same areas. As can be seen in Fig. 7(a), the original texture in the as-annealed sample, i.e. the Cube and the C components, can still be observed on the ODF maps of the sample subjected to the strain ε of 0.45 with volume fractions of 4.57% and 3.64%, respectively.

It is well known that texture is essentially a cluster of crystallographic orientations with close Euler angles. At the strain ε of 0.90, different colour aggregations on the EBSM map represent the variety of texture components. Accordingly, the volume fractions of all ideal components with the exception of Cube and C increase many-fold. The preferred orientations have been rotated to the positions of B/B_b, whose volume fraction accounts for about 5.5%. Most of the B/B_b texture components have already been transformed into the components of C (3.16%) and A* 2 (6.97%) when the strain ε increases to 1.34. At a strain ε of 2.69, the prevalence of the C and A* 2 components has been replaced by the newly developed B/B_b (3.19%), A* 1 (1.88%) and A/A_b (5.30%) components. The high subdivision of the elongated grains into smaller grains should be responsible for the decreases of the C and A* 2 components [51].

At the strain ε of 5.38 and 10.7, significant grain elongation occurs once again. It follows that the volume fraction of the C component progressively increases to 1.52% and 5.81% at the two stages, respectively. In addition to the C component, the volume fraction of A* 1component drops sharply from 4.81% to 0.4%, while that of A* 2 component demonstrates a reverse trend and increases significantly from 0.41% to 3.52% when the strain ε increases from 5.38 to 10.7. With the increase in strain ε to 21.51, the subdivision of grains leads to the emergence of new predominant texture components, A/A_b (6.92%) and B/B_b (2.75%). At $\varepsilon = 32.27$ and 53.78, the composition of major components is the same although their volume fractions vary slightly with the increase of strain. Fur-

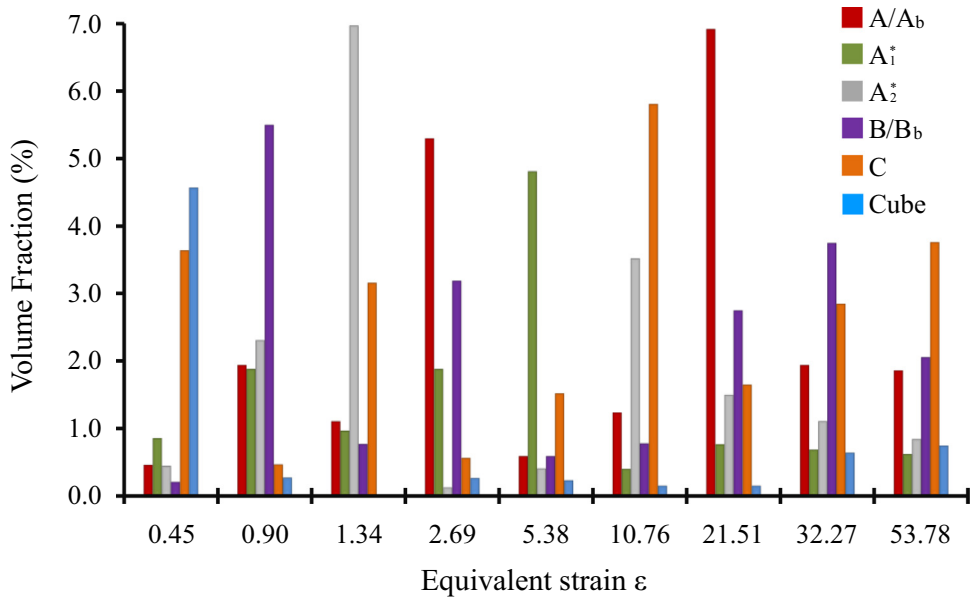

Fig. 8 – Volume fractions of ideal simple-shear orentations on the HPT samples at different deformation stages.

ther deformation causes more divergent orientation rotation. As shown in Fig. 7(h) and (i), the orientation spread is promoted and the crystallographic orientations which occupy the positions of B/B_b, A* 1 and A* 2 rotate away gradually when the strain ε increases from 32.27 to 53.78. The saturation of grain size implies the achievement of typical simple shear components at the two stages. It is known that for a high SFE FCC material, the typical simple shear texture is composed of a strong B fibre (A/A_b, B/B_b and C) and a less strong A fibre (A* 1, A* 2 and A/A_b) [52]. This is in good agreement with the current measurements on texture components. In addition, it is found that the C orientation can remain stable at large strains.

4. Discussion

4.1. *Microstructure evolution*

In this study, it is found that grain refinement is not a linear function of the shear strain in HPT. For example, when the equivalent strain ε increases from about 3–11, the grain size is stable although the increase in shear strain at this stage approximates the cumulative strain of all previous stages. Significant grain refinement mainly takes place during two stages. One stage is in the equivalent strain range from ~0 to 1, and the other from ~11 to 32. For $\varepsilon >$ ~32, saturation of grain refinement is achieved.

Generally, the microstructure evolution during the HPT process can be roughly divided into two different stages: fragmentation and saturation [20]. In the present study, however, detailed observations demonstrate that the so-called fragmentation stage actually comprises many sub-stages of grain fragmentation and elongation. The major microstructural evolution of the grain fragmentation and elongation is schematically demonstrated in Fig. 9. The black line and the blue line represent the HAGB and LAGB, respectively. During the fragmentation process, the parent grains are subdivided into smaller grains with low intra-granular dislocation density [53]. Thus their grain size decreases dramatically. During the process of elongation, the grains formed as a result of the fragmentation process are elongated without severe fragmentation, and the dislocation density inside these grains rises significantly, leading to the emergence of new intra-granular LAGBs owing to dislocation mutual reaction. With further deformation, these intra-granular LAGBs are converted into HAGBs by absorbing dislocation, representing the onset of new fragmentation process. The two processes occur alternatively until the saturation stage where the dislocation formation is balanced with dislocation absorption [43]. Noteworthy, because of the coexistence of elongated grains and new-born grains, the two processes are not mutually exclusive at the same stage. For example, the equivalent strain of $0.90 < \varepsilon < 1.34$ is a combination stage of grain fragmentation and elongation, while the equivalent strain of $1.34 < \varepsilon < 2.69$ and $2.69 < \varepsilon < 5.38$ are the stages at which the fragmentation process and the elongation process are dominant, respectively.

4.2. *Lattice rotation retardation at steady-state stage*

It is generally considered that the development of torsional texture is considerably complicated. All parts of the cylindrical sample except the axis are continuously rotated during the entire torsional deformation process. As a result, a stable texture is rarely observed in torsional deformation and the strength of the torsional texture is generally less than that of plane strain or axisymmetric deformation texture. Oscillation in texture is expected due to the periodic change in SD. This deduction is consistent with the simulation on the simple shear process [54]. In the present study, however, although the orientation spread ascends with increasing strain, it is found that the texture pattern does not change very much from a strain ε of 32.27 onwards.. The texture stability is also observed

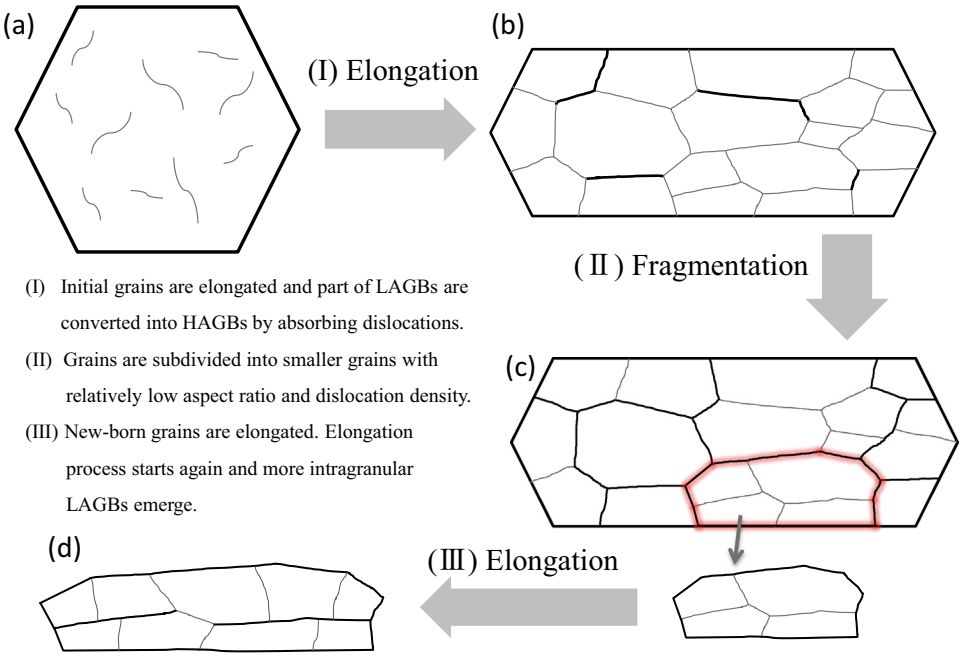

Fig. 9 – Schematic diagram of the grain elongation process and fragmentation process in Al during HPT.

in other HPT experiments at steady-state stages where UFG or NC structures are achieved, which is considered as an apparent effect [55,56]. The mechanism of dynamic equilibrium is probably the main reason for the apparent effect, i.e. a balance is established between texture component formation and disappearance. In addition, texture development is linked with lattice rotation [57,58]. Accordingly, the factors that affect the lattice rotation will necessarily play certain roles in the texture evolution. In this section, the dependence of the lattice rotation rate on the grain size at steady-state stage is discussed.

The development of texture essentially involves diverging grain rotation. A grain fragmentation model proposed by Toth et al. successfully simulated the torsional texture [59]. The model is based on the assumption that a grain lattice rotation within an individual grain is impeded by friction from its neighbouring grains. As a result, the rotated grain could be divided into two layers. The deformation of outer layer adjacent to the GB gives rise to dislocation activities and the concomitant lattice distortion. The inner layer not influenced by the GB could be considered as a rigid body. The dislocation activities gradually become weak as the grain size reduces to the nano scale. Dislocation sources and pile-ups are hardly expected in materials tens of nanometres in grain size, due to limited grain size and higher density of GBs [60], so that the distortion layer is negligible in this case. Moldovan et al. [61] proposed a model to investigate the grain rotation driven by diffusion in the materials with tens of nanometre size. In the model a grain could be regarded as a rigid body due to its negligible distortion layer, and the rigid body rotation is a viscous process. In the present study, the grain shapes are seen to become relatively equiaxed and the average grain size is stabilized from a strain ε of ~32 onwards. Generally speaking, the most severe distortion occurs at the grain fringes [62]. The HPT experiment revealed that although high geometrically necessary dislocation (GND) density can be found within some grains, the lattice curvatures of UFG materials are absent overall at the steady-state stage [45]. This indicates that the distorted regions are narrow and that the texture of grains mainly depends on the orientation of inner regions which are not affected by distortion. Therefore, the narrow deformation zone at the thin outer layer could be neglected without large deviations. Furthermore, the periodic change of the shear direction at constant angular velocity gives rise to the continuous lattice rotation during HPT deformation. Following the arguments presented above, the constraining effect of grain rotation with respect to its surrounding grains could be modelled in terms of rotational friction for a spherical body with the viscous GB-sliding condition rotating with a constant angular velocity. The frictional force F is calculated by a modified equation [63]:

$$\mathbf{F} = -4\pi\mu R\nu \tag{3}$$

where μ is the dynamic viscosity, R is the radius of the sphere and $\boldsymbol{\nu}$ is the rotation velocity.

The sphere rotation is retarded due to an angular acceleration α resulting from the frictional force F:

$$\alpha = \frac{\mathbf{M}}{I} = \frac{\mathbf{R}\times\mathbf{F}}{I} = -\frac{15\mu}{2\rho R^3}\boldsymbol{\nu}\times\mathbf{n} \tag{4}$$

where $\mathbf{M}$ is the frictional torque on the sphere, I is the rotational inertia of the sphere, ρ is the density and $\mathbf{n}$ is a unit vector normal to the surface.

The frictional angular deceleration hinders the lattice rotation. According to Eq. (4), it is clear that the angular acceleration α increases with a reduction in grain size. As a result, the development of texture is retarded. It is noteworthy that in practice, lattice rotation could be effected by many factors such as grain shape and temperature, apart from grain

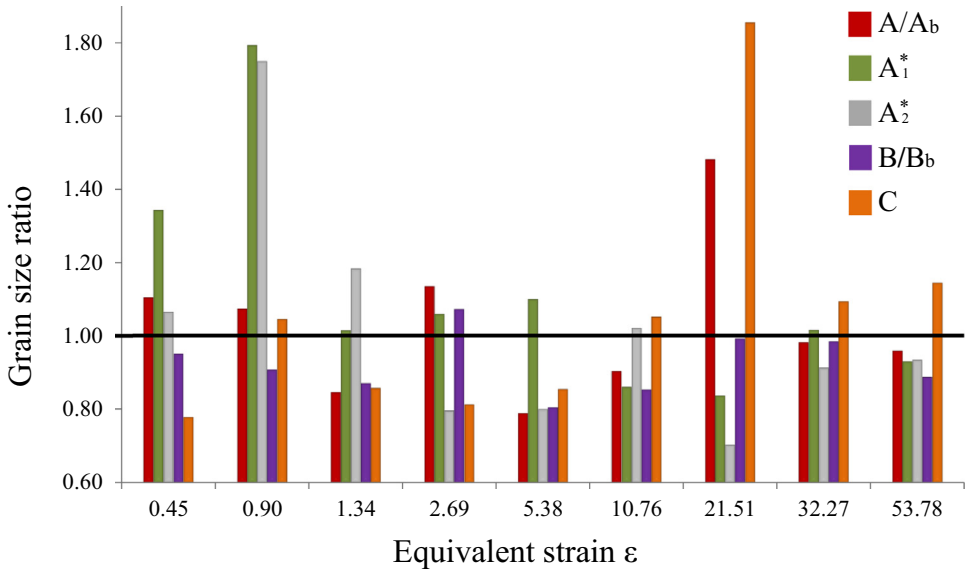

Fig. 10 – The grain size ratio of ideal components at different deformation stages.

size. In addition, the influence of grain size on lattice rotation varies for different grain size ranges. When the grain size drops further to dozens of nanometres, the activation of lattice diffusion owing to higher density of GBs could accelerate lattice rotation [61].

4.3. *Sensitivity of fragmentation to grain orientation*

The resistance of grains to subdivide depending on their orientation is expected in torsional deformation. Specifically, it is widely believed that the orientation gradients in ideally oriented grains are generally less than those in the grains at non-ideal positions. This behaviour could be explained by the model of crystallographic rotation field for torsion [64–66]. According to the model, the orientations away from ideal positions have high lattice rotation rates, whereas the lattice rotation rates approach zero for orientations close to ideal positions. It is well known that the subdivision of a grain is due to the diverging rotation of its adjacent parts. As a result of different lattice rotation rates, ideal orientations could be sustained over relatively appreciable strains, and non-ideal orientations are prone to fragmentation.

In this study, the grain size ratio is defined as the ratio of the average grain size of a certain component to the average grain size at the same strain level. The grain size ratios of ideal simple shear components at different stages are shown in Fig. 10. For a stable orientation, the grain size ratio is theoretically greater than 1. In Fig. 10, it is found that the ideal components do not demonstrate any regularly fragmentation-resistant behaviour at the first two stages. This is possibly because monoclinic symmetry has not been yet fully achieved at the preliminary stages. With increased deformation, an apparent correlation between the grain size ratio and the volume fraction of simple shear components (*cf.* Fig. 8) is detected for the strain range of 1.34 to 21.51. Specifically, the grain size ratio of a component is proportional to its volume fraction in most cases. The components with high volume fractions generally have high grain size ratios. However, not all the grains oriented near ideal positions are less refined than other grains. The average grain sizes of weak components are mostly smaller, indicating that the resistance of a component to fragmentation is sensitive to its volume fraction. From the strain ε of 32.27 onwards, the influence of orientation on fragmentation is gradually diminished with the exception of the C component when the average grain size falls to the nanometre level. This is in good agreement with a previous observation [28]. This behaviour could be explained by the influence of grain size. As stated before, intra-granular orientation gradients become very small at this grain size level. The absence of high intra-granular orientation gradient prevents the subdivision of all grains. As a result, the discrepancies of fragmentation between ideal components and non-ideal components tend to diminish and the sensitivity of fragmentation to grain orientation gradually decreases. The high resistance to fragmentation of the C component is possibly associated with its self-symmetry [27]. Further evidence can be sought for in future studies.

5. Conclusion

In this paper, the evolution of microstructural characteristics and texture of the HPT-processed CP Al were studied. The research findings can be summarised as follows:

1 Grain refinement is not a linear function of the shear strain in HPT. Significant grain refinement mainly takes place in two stages, i.e. the equivalent strain of $\sim 0 < \varepsilon < 1$ and $\sim 11 < \varepsilon < 32$. For a strain $\varepsilon > \sim 32$, saturation of grain refinement is achieved.
2 Grain fragmentation and grain elongation are two important aspects of microstructural evolution before attainment of steady state during HPT deformation. The grain fragmentation and grain elongation appear alternately until the saturation stage.

3 The lattice rotation of UFG materials involves grain size in the steady-state stage, in which the development of texture is slowed down with decreasing grain size.
4 The strong simple shear components generally have larger grain size than weak simple shear components and non-ideal components. The resistance of an ideal component to fragmentation is related with its volume fraction. The sensitivity of fragmentation to grain orientation diminishes in the steady-state stage.

Conflicts of interest

The authors declare no conflicts of interest.

Acknowledgements

This work is supported by the Natural Science Foundation of Hebei Province, China, under Grant No. E2019210036, ARC Discovery Project DP170103092 and the UOW Electron Microscopy Centre.

REFERENCES

[1] Hall E. The deformation and ageing of mild steel: III discussion of results. Proc Phys Soc Sect B 1951;64(9):747.
[2] Petch N. The cleavage strengh of polycrystals. J. of the Iron and Steel Inst 1953;174:25–8.
[3] Lee H-J, et al. Significance of grain refinement on microstructure and mechanical properties of an Al-3% Mg alloy processed by high-pressure torsion. J Alloys Compd 2016;686:998–1007.
[4] Liu Q, et al. Microstructure and mechanical properties of ultra-fine grained MoNbTaTiV refractory high-entropy alloy fabricated by spark plasma sintering. J Mater Sci Technol 2019;35(11):2600–7.
[5] Yan S, et al. Microstructure evolution and flow localization characteristics of 5A06 alloy in high strain rate forming process. Procedia Eng 2014;81:1198–203.
[6] Fu B, et al. High strength-ductility nano-structured high manganese steel produced by cryogenic asymmetry-rolling. J Mater Sci Technol 2018;34(4):695–9.
[7] Lu Q, et al. Simultaneously enhanced strength and ductility of 6xxx Al alloys via manipulating meso-scale and nano-scale structures guided with phase equilibrium. J Mater Sci Technol 2019.
[8] Matsunoshita H, et al. Ultrafine-grained magnesium–lithium alloy processed by high-pressure torsion: low-temperature superplasticity and potential for hydroforming. Mater Sci Eng A 2015;640:443–8.
[9] Alizadeh R, et al. Superplasticity of a nano-grained Mg–Gd–Y–Zr alloy processed by high-pressure torsion. Mater Sci Eng A 2016;651:786–94.
[10] Kwak TY, Kim WJ. Superplastic behavior of an ultrafine-grained Mg-13Zn-1.55Y alloy with a high volume fraction of icosahedral phases prepared by high-ratio differential speed rolling. J Mater Sci Technol 2017;33(9):919–25.
[11] Yu H, et al. Fabrication of nanostructured aluminum sheets using four-layer accumulative roll bonding. Mater Manuf Process 2014;29(4):448–53.
[12] Qian C-h, Li P, Xue K-m. Thermal properties of SiCp/Al composites consolidated by equal channel angular pressing and torsion. J Mater Eng Perform 2015;24(2):832–8.
[13] Yu HL, et al. Special rolling techniques for improvement of mechanical properties of ultrafine-grained metal sheets: a review. Adv Eng Mater 2016;18(5):754–69.
[14] Qian C-h, Ping L, Xue K-m. Influence of deformation passes on interface of SiCp/Al composites consolidated by equal channel angular pressing and torsion. Trans Nonferrous Met Soc China 2015;25(5):1376–82.
[15] Edalati K, et al. Effect of temperature rise on microstructural evolution during high-pressure torsion. Mater Sci Eng A 2018;714:167–71.
[16] Lanjewar H, et al. Statistical analysis of dislocation substructure in commercially pure aluminum subjected to static and dynamic high pressure torsion. Mater Charact 2019:110088.
[17] Lanjewar H, et al. Severe plastically deformed commercially pure aluminum: substructure, micro-texture and associated mechanical response during uniaxial tension. Mater Sci Eng A 2019;764:138195.
[18] Lanjewar HA, et al. Miniature tensile testing of SPD processed fine-grained aluminum. In: In journal of physics: conference series. IOP Publishing; 2019.
[19] Cao Y, et al. Concurrent microstructural evolution of ferrite and austenite in a duplex stainless steel processed by high-pressure torsion. Acta Mater 2014;63:16–29.
[20] Pippan R, et al. Saturation of fragmentation during severe plastic deformation. Annu Rev Mater Res 2010;40:319–43.
[21] Renk O, et al. Direct evidence for grain boundary motion as the dominant restoration mechanism in the steady-state regime of extremely cold-rolled copper. Acta Mater 2014;77:401–10.
[22] Orlov D, Kamikawa N, Tsuji N. High pressure torsion to refine grains in pure aluminum up to saturation: mechanisms of structure evolution and their dependence on strain. Philos Mag 2012;92(18):2329–50.
[23] Naghdy S, et al. Evolution of microstructure and texture in commercial pure aluminum subjected to high pressure torsion processing. Mater Charact 2016;120:285–94.
[24] Tidu A, Heizmann J-JJT. Correlation beetween size-strain pole and figure and texture. Stress and Microstructure 1991;14:79–84.
[25] Raabe DJpss. Simulation and experimental examination of the evolution of orientation gradients in single grains during rolling of body centered cubic polycrystals 1994;181(2):291–9.
[26] Delannay L, et al. Quantitative analysis of grain subdivision in cold rolled aluminium. Acta Mater 2001;49(13):2441–51.
[27] Quey R, Dawson PR, Driver JH. Grain orientation fragmentation in hot-deformed aluminium: experiment and simulation. J Mech Phys Solids 2012;60(3):509–24.
[28] Naghdy S, et al. Morphological and crystallographic anisotropy of severely deformed commercially pure aluminium by three-dimensional electron backscatter diffraction. J Appl Crystallogr 2017;50(5):1512–23.
[29] Liao X, et al. High-pressure torsion-induced grain growth in electrodeposited nanocrystalline Ni. Appl Phys Lett 2006;88(2):021909.
[30] Wen H, et al. High-pressure torsion-induced grain growth and detwinning in cryomilled Cu powders. Philos Mag 2010;90(34):4541–50.
[31] Shrivastava SC, Jonas JJ, Canova G. Equivalent strain in large deformation torsion testing : theoretical and practical considerations. J Mech Phys Solids 1982;30(1):75–90.
[32] Zhilyaev AP, et al. Experimental parameters influencing grain refinement and microstructural evolution during high-pressure torsion. Acta Mater 2003;51(3):753–65.
[33] Zhilyaev AP, McNelley TR, Langdon TG. Evolution of microstructure and microtexture in fcc metals during high-pressure torsion. J Mater Sci 2007;42(5):1517–28.

[34] Valiev RZ, et al. Structure and deformaton behaviour of Armco iron subjected to severe plastic deformation. Acta Mater 1996;44(12):4705–12.
[35] Wetscher F, et al. TEM investigations of the structural evolution in a pearlitic steel deformed by high-pressure torsion. Metall Mater Trans A 2006;37(6):1963–8.
[36] Valiev RZ, et al. Producing bulk ultrafine-grained materials by severe plastic deformation. JOM 2006;58(4):33–9.
[37] Stüwe HP. Equivalent strains in severe plastic deformation. Adv Eng Mater 2003;5(5):291–5.
[38] Canova GR, Kocks UF, Jonas JJ. Theory of torsion texture development. Acta Metall 1984;32(2):211–26.
[39] Toth L, Gilormini P, Jonas J. Effect of rate sensitivity on the stability of torsion textures. Acta Metall 1988;36(12):3077–91.
[40] Jahedi M, et al. Texture evolution and enhanced grain refinement under high-pressure-double-torsion. Mater Sci Eng A 2014;611:29–36.
[41] Korznikova EA, et al. Microstructural evolution and electro-resistivity in HPT nickel. Mater Sci Eng A 2012;556:437–45.
[42] Liu Q, Juul Jensen D, Hansen N. Effect of grain orientation on deformation structure in cold-rolled polycrystalline aluminium. Acta Mater 1998;46(16):5819–38.
[43] Ito Y, Horita Z. Microstructural evolution in pure aluminum processed by high-pressure torsion. Mater Sci Eng A 2009;503(1):32–6.
[44] Xu C, Horita Z, Langdon TG. The evolution of homogeneity in processing by high-pressure torsion. Acta Mater 2007;55(1):203–12.
[45] Pougis A, et al. Extension of the Derby relation to metals severely deformed to their steady-state ultrafine-grain size. ScriptaMater 2014;72:59–62.
[46] Cahn JW, Mishin Y, Suzuki A. Coupling grain boundary motion to shear deformation. Acta Mater 2006;54(19):4953–75.
[47] Homer ER, et al. Phenomenology of shear-coupled grain boundary motion in symmetric tilt and general grain boundaries. Acta Mater 2013;61(4):1048–60.
[48] Li CH, et al. Stress-induced movement of crystal boundaries. Acta Metall 1953;1(2):223–9.
[49] Arzaghi M, et al. Microstructure, texture and mechanical properties of aluminum processed by high-pressure tube twisting. Acta Mater 2012;60(11):4393–408.
[50] Cortie M. Calculation of texture volume fractions by integration and Gaussian fitting. Texture Stress Microstruct 1997;29(3-4):155–83.
[51] Montheillet F, Gilormini P, Jonas J. Relation between axial stresses and texture development during torsion testing: a simplified theory. Acta Metall 1985;33(4):705–17.
[52] Kocks UF, Tomé CN, Wenk H-R. Texture and anisotropy: preferred orientations in polycrystals and their effect on materials properties. Cambridge university press; 2000.
[53] Inoue T, et al. Effect of initial grain sizes on hardness variation and strain distribution of pure aluminum severely deformed by compression tests. Acta Mater 2008;56(20):6291–303.
[54] Cho J-H, Dawson PRJM, M.T. A. Investigation on texture evolution during friction stir welding of stainless steel. MetallMater Trans 2006;37(4):1147–64.
[55] Korznikova E, et al. Microstructural evolution and electro-resistivity in HPT nickel. Mater Sci Eng A 2012;556:437–45.
[56] Al-Fadhalah KJ, et al. Microstructure and microtexture in pure copper processed by high-pressure torsion. J Mater Sci 2013;48(13):4563–72.
[57] Toth L, et al. Length changes during free end torsion: a rate sensitive analysis. Int J Plast 1990;6(1):83–108.
[58] Beausir B, Tóth LS, Neale KW. Ideal orientations and persistence characteristics of hexagonal close packed crystals in simple shear. Acta Mater 2007;55(8):2695–705.
[59] Tóth LS, et al. A model of grain fragmentation based on lattice curvature. Acta Mater 2010;58(5):1782–94.
[60] Shan Z, et al. Grain boundary-mediated plasticity in nanocrystalline nickel. Science 2004;305(5684):654–7.
[61] Moldovan D, Wolf D, Phillpot SR. Theory of diffusion-accommodated grain rotation in columnar polycrystalline microstructures. Acta Mater 2001;49(17):3521–32.
[62] Mishra S, et al. On the widths of orientation gradient zones adjacent to grain boundaries. Scripta Mater 2009;61(3):273–6.
[63] Hu CM, Zwanzig RJTJoCP. Rotational friction coefficients for spheroids with the slipping boundary condition. J ChemPhys 1974;60(11):4354–7.
[64] Tóth L, Neale K, Jonas JJAM. Stress response and persistence characteristics of the ideal orientations of shear textures. Acta Metall 1989;37(8):2197–210.
[65] Jonas JJIjoms. Modelling the length changes that take place during torsion testing. Int J Mech Sci 1993;35(12):1065–77.
[66] Barnett M, Montheillet FJAm. The generation of new high-angle boundaries in aluminium during hot torsion. Acta Mater 2002;50(9):2285–96.